Global heat flow trends resolved from multiple geological and geophysical proxies

B. Goutorbe, Jeffrey Poort, F. Lucazeau, S. Raillard

Geophysical Journal International

Geophys. J. Int. (2011) **187,** 1405–1419 doi: 10.1111/j.1365-246X.2011.05228.x

Global heat flow trends resolved from multiple geological and geophysical proxies

B. Goutorbe,[1]* J. Poort,[1]† F. Lucazeau[1]§ and S. Raillard[2]

[1] *Géosciences Marines, Institut de Physique du Globe de Paris, Paris, France. E-mail: goutorbe@hotmail.com*
[2] *Deeply Buried Reservoirs Research Project, Total, CSTJF, Pau, France*

Accepted 2011 September 8. Received 2011 August 15; in original form 2010 October 29

SUMMARY

Because global coverage of heat flow measurements is still poor in many areas, empirical estimators based on the geology, the thermotectonic age or the velocity structure of the upper mantle have often been used to affect an estimate to regions where such measurements are absent. On the basis of the assumption that heat flow is strongly related to its geodynamic environment, one may integrate multiple proxies derived from a large body of global geological and geophysical data sets assembled during the past decades; these should help to better capture the variety of present-day settings. This idea is illustrated through two simple empirical methods: both of them are based on a set of examples, where heat flow measurements are associated with relevant terrestrial observables such as surface heat production, upper-mantle velocity structure, tectono-thermal age, on a $1^\circ \times 1^\circ$ grid. To a given target point owning a number of observables, the methods associate a heat flow distribution rather than a deterministic value to account for intrinsic variability and uncertainty within a defined geodynamic environment. The 'best combination method' seeks the particular combination of observables that minimizes the dispersion of the heat flow distribution generated from the set of examples. The 'similarity method' attributes a weight to each example depending on its degree of similarity with the target point. The methods are transparent and are able to handle sets of observables that are not available over the whole Earth (e.g. heat production). The resulting trends of the mean heat flow deduced from the two methods do not differ strongly, but the similarity method shows a better accuracy in cross-validation tests. These tests suggest that the selected proxies have the potential to recover at least partly medium- to large-scale features of surface heat flow. The methods depict the main global trends of low heat flow in stable and ancient regions, and thermal high in active orogens and rift zones. Broad thermal anomalies are outlined in the Sahara and in the tectonically active eastern part of Antarctica. The similarity method estimates a continental heat loss of 13.6 ± 0.8 TW (2σ uncertainty), which is consistent with previous estimates.

Key words: Spatial analysis; Heat flows.

1 INTRODUCTION

Terrestrial heat flow is a crucial parameter to constrain the thermal structure of the lithosphere, the global heat loss of the Earth, and models of thermomechanical evolution of the lithosphere (encountered, e.g. in industrial basin modelling studies). Heat flow is measured at the surface, using most often temperature logs and thermal conductivity measurements (or estimates) in deep boreholes, and gravity-driven thermal probes in soft lake or ocean sediments. As these methods are still time intensive and technically challenging, heat flow measurements cover only a limited surface of the Earth.

A global heat flow compilation published by the International Heat Flow Commission (Pollack *et al.* 1993) now counts more than 22 000 stations (IHFC 2009). Other versions of this database have been updated and further completed with exploration heat flow data (Artemieva & Mooney 2001; Davies & Davies 2010, and other unpublished databases) and include now up to 38 000 unique heat flow sites worldwide. Despite these large numbers, the distribution over the globe is very heterogeneous and many areas remain poorly

*Now at: Instituto de Geociências Universidade Federal Fluminense Niterói, Brazil.
†Now at: Institut des Sciences de la Terre de Paris, Université Pierre et Marie Curie, Paris, France.
§Now at: Dynamique des Fluides Géologiques, Institut de Physique du Globe de Paris, Paris, France.

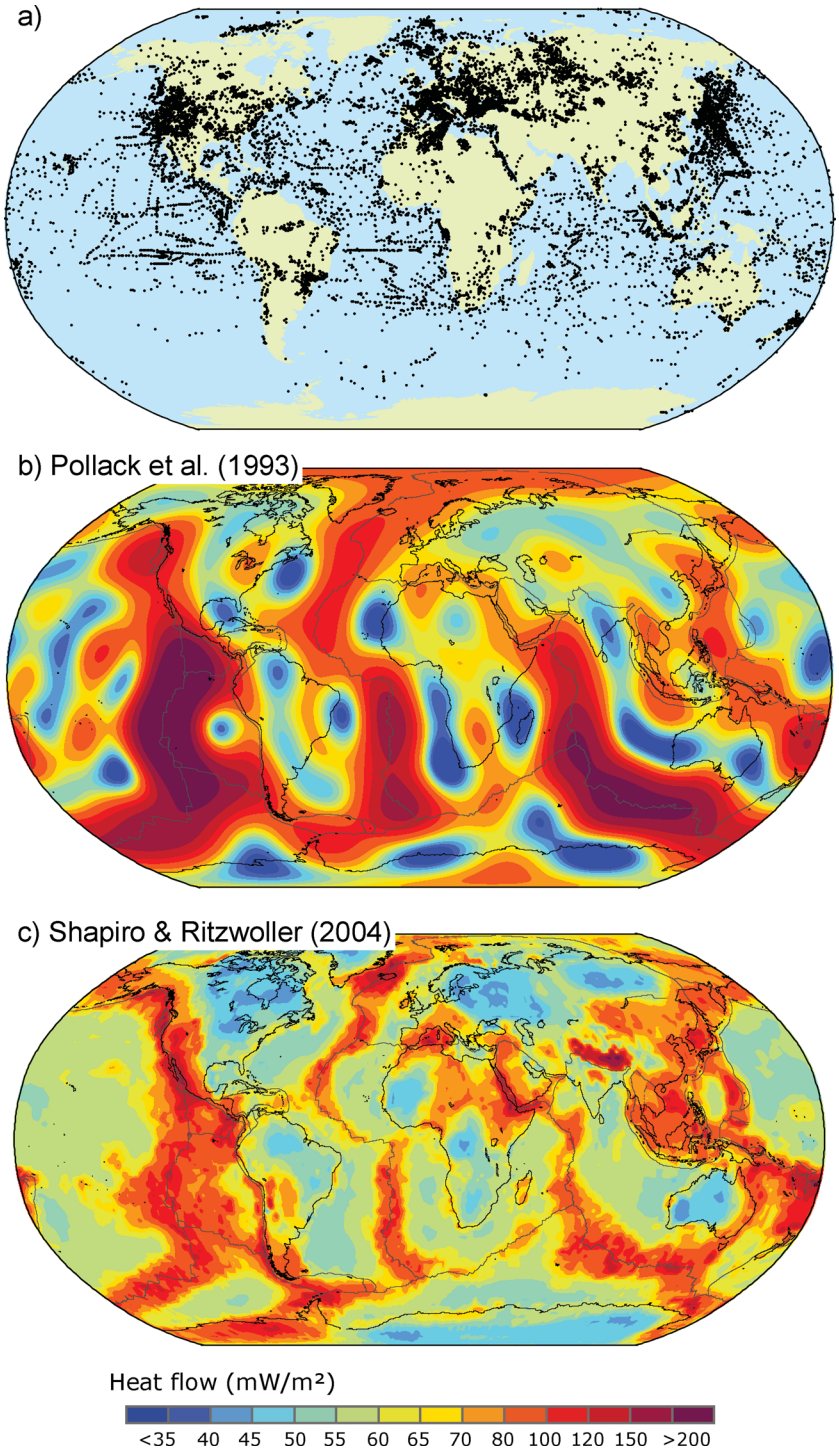

Figure 1. (a) Global heat flow data set, including now up to 34 500 sites (note uneven sampling and poor coverage in many areas); (b, c) published efforts to extrapolate heat flow using an estimator based on the thermotectonic age and the surface geology (Pollack *et al.* 1993) (b); or on a shear velocity model of the crust and upper mantle (Shapiro & Ritzwoller 2004) (c). In the former study, heat flow measurements in Cenozoic oceanic crust were replaced by values derived from the GDH1 model (Stein & Stein 1992), which explains the large differences between the two maps along oceanic ridges. Robinson projection (also used in subsequent figures). See the electronic edition of the Journal for a colour version of this figure.

covered (Fig. 1a). Using averages over 1° × 1° windows, only 12 per cent of the continents and 19 per cent of the oceans are sampled. Moreover, the quality of the heat flow data is highly variable and a data quality filtering may strongly reduce the number of values and the global coverage.

For this reason, many studies sought control parameter(s) to extrapolate heat flow to regions where no measurement exists. In the oceanic domain, the observation that heat flow and bathymetry decrease as the ocean floor spreads away from the ridge led to the development of age-dependent physical models for the thermal

evolution of the lithosphere: these essentially represent the conductive cooling of an initially hot material subjected to a cold upper boundary condition (e.g. Davis & Lister 1974; Crough 1975; Parsons & Sclater 1977; Stein & Stein 1992). Compared to measured heat flow in the oceans, the predictions of the models fit well for oceanic ages older than 50 Myr. For younger oceanic crust, a lower and highly dispersed measured heat flow is attributed to the effect of hydrothermal circulation and oversampling in areas of fluid recharge (Stein & Stein 1994; Elderfield *et al.* 2004).

On the continents, similar analysis tried to relate heat flow to the thermotectonic age of the crust and the lithosphere (Vitorello & Pollack 1980). There is a general trend of decreasing heat flow with increasing age, but the relation is weak and inadequate in many areas (Rao *et al.* 1982; Morgan 1984; Jaupart & Mareschal 2007). The reason is that continental heat flow contains a large and variable radiogenic component, in addition to a possible transient component related to local 'thermotectonic' events. All components vary within different geodynamic settings, and the exact contribution of each of them, in most of these settings, is still hard to constrain. Therefore, extrapolation efforts on the continents have been focused on empirical approaches. For example, Chapman & Pollack (1975) and Pollack *et al.* (1993) used an estimator based on the thermotectonic age and some geological characteristics, and then provided a spherical harmonics representation of degree and order 12 (Fig. 1b). As this represents only large wavelength variations of more than 3000 km, it does not show regional heat flow details. In the continuity of the aforementioned studies, Davies & Davies (2010) introduced geographic information system (GIS) methods to average heat flow by geological domain. As an alternative approach, Shapiro & Ritzwoller (2004) worked out a global extrapolation guided by a shear velocity model of the upper mantle (Fig. 1c). By construction, this approach is similarly only sensitive to the large-scale spatial variations of heat flow.

Of course, empirical extrapolations will never replace actual measurements of heat flow and crustal heat production; but one may assume that surface heat flow is directly related to the geology of the crust and the geodynamic context, and that the global coverage of heat flow measurements already represents a large variety of present-day geological and geodynamic settings. In other words we assume that, to some extent, existing values may be transposed to regions of similar geological context. With this objective in mind, it is possible to take advantage of the numerous global geological and geophysical data sets that were built up and released during the past decades. The basic ideas are that multiple proxies should better characterize the variety of geodynamic environments; and that surface heat flow will be more efficiently retrieved from all available information rather than from a single estimator, since each proxy is only partly related to the thermal state of the lithosphere. In this paper, we explore these ideas through two simple empirical approaches of heat flow extrapolation: instead of using a single parameter to reference a heat flow estimator (like in previous studies, thermotectonic age, surface geology or seismic velocity), the suggested approaches incorporate a large set of relevant observables from available global maps and compilations. In practical, heat flow data are combined with the corresponding terrestrial observables to form a data set of examples. A heat flow distribution is then associated with any target point, from elements of the latter data set: the 'best combination method' seeks the particular combination of observables, which minimizes the dispersion of the generated heat flow distribution, while the 'similarity method' affects a weight to each example depending on its degree of similarity with the target point. We describe in the next section the data sets of heat flow and other terrestrial observables used in this study, and the procedure to build-up the set of examples. The description and predictions of the extrapolation methods are then presented and discussed.

2 GLOBAL DATA SETS

2.1 Heat flow data

The heat flow data come from an updated version of the global database of Pollack *et al.* (1992). The database now includes ∼34 500 heat flow measurements, 16 000 of which are located in emerged continental domain and 18 500 in marine domain (Fig. 1a). (A version of the database is available online at http://www.ipgp.fr/∼lucazeau/NGHF.kmz.) To address the problems of strong variability of heat flow at small scale (Fig. 2, left-hand side), uneven distribution of measurements and scale difference between point measurements and global observables, we worked on a $1^\circ \times 1^\circ$ grid; such a grid is not equal-area, but it is more straightforward to assemble and process, and the methods suggested thereafter should not be strongly sensitive to the variations in area of the grid cells. The processing consisted of (1) excluding all continental measurements lower than 20 mW m^{-2} or higher than 150 mW m^{-2}, which are likely to be affected by surface processes, (2) filling a $1^\circ \times 1^\circ$ grid with the median value of heat flow within each cell and (3) smoothing the obtained grid using a Gaussian filter (i.e. with Gaussian-shaped weights around each cell). The resulting map unveils a partial image of the heat escaping through the Earth's surface (Fig. 2, right-hand side; see also the online supplementary material).

2.2 Terrestrial observables

We incorporated a set of more than 20 estimators derived from global geological and geophysical observations and models (Table 1, and online supplementary material). The selected terrestrial observables are directly or indirectly related to the thermal processes in the crust and the mantle, and may thus help to constrain the different contributions to the surface heat flow. For example, mantle seismic velocities are affected by the temperature of the mantle, while heat production and thickness of the crust are related to the crustal heat flow component. Other observables are affected by both components (e.g. topography and tectonothermal age), and by geodynamic transient effects (e.g. volcanoes and rifts). Obviously, it should be understood that the proxies are imperfect, in the sense that none is solely sensitive to the thermal state of the lithosphere: the relation of each of them with heat flow can be considerably obscured by additional, non-thermal effects; our objective is to extract a significant part of the thermal signal by incorporating a large number of estimators. Three types of observables are distinguished.

(1) 'Continuous observables', which belong to the real continuum (e.g. Moho depth or age of the ocean floor);
(2) 'Classes', which take on a finite number of discrete values (e.g. geological province or basin type);
(3) 'Distances', which represent the distance to the closest element of a given feature (e.g. distance to the closest oceanic ridge).

The geological and geophysical data sets, used to build-up the proxies, were collected from publicly available global compilation,

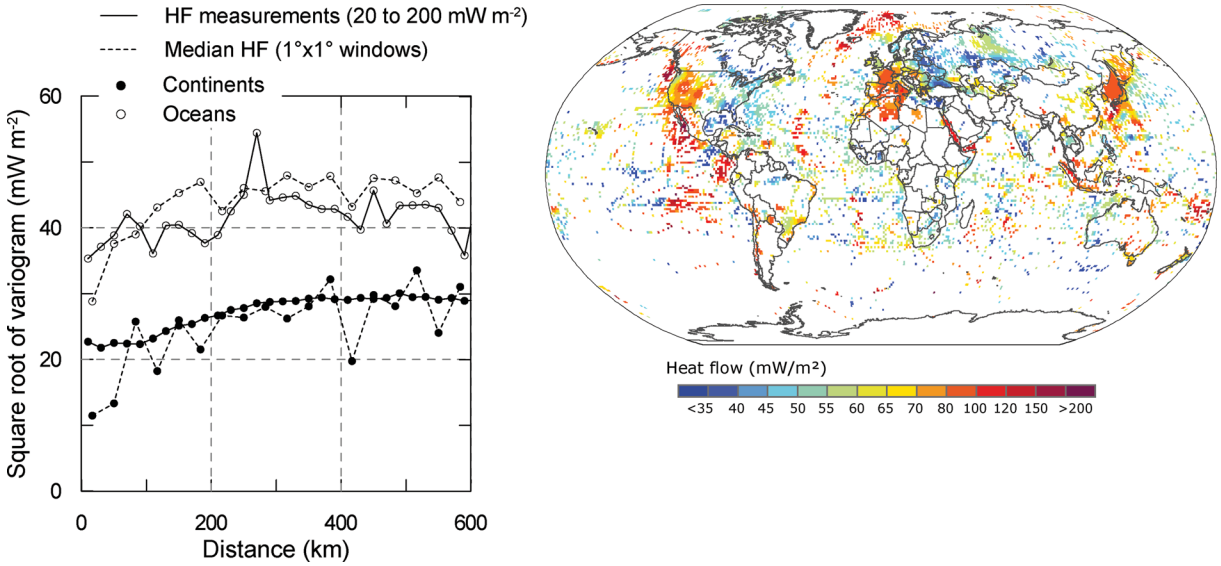

Figure 2. (Left-hand side) Semivariogram of heat flow data, illustrating the short-scale spatial variability as it does not tend to zero at small distances; note that taking the median value in $1^\circ \times 1^\circ$ windows, without further smoothing, does not remove all small-scale variability. (Right-hand side) $1^\circ \times 1^\circ$ global heat flow grid used in the set of examples; a Gaussian filter with a 500 km radius was applied to smooth statistically unexplained small-scale variations [with radius of filter defined as three times the conventional Gaussian sigma, see command `grdfilter` from the Generic Mapping Tools (Wessel & Smith 1991)]. This heat flow grid is available in the online supplementary material. See the electronic edition of the Journal for a colour version of this figure.

Table 1. List of the terrestrial proxies used in the new guided heat flow extrapolation. The source data used to build-up the observables are discussed in detail in Section 2.2. The non-confidential proxies are available in the online supplementary material.

Observable	Source
Continuous observables	
Heat production (median grid)	Global database
Heat production provinces	New model
Thickness of upper crust	CRUST2.0 (Bassin *et al.* 2000)
Thickness of middle crust	CRUST2.0 (Bassin *et al.* 2000)
Upper-mantle density anomaly	Kaban *et al.* (2004)
Topography	ETOPO-2 (NOAA 2006)
Age of ocean floor	Müller *et al.* (2008)
Thickness of lithosphere	derived from Shapiro & Ritzwoller (2002)
Gradient of lithosphere thickness	derived from Shapiro & Ritzwoller (2002)
Sediment thickness	Laske & Masters (1997)
Age of basin top	TOTAL
Age of basin bottom	TOTAL
Age of rift initiation	Şengör & Natal'in (2001) and TOTAL
Age of rift termination	Şengör & Natal'in (2001) and TOTAL
Class observables	
Upper-mantle velocity structure	derived from Shapiro & Ritzwoller (2002)
Age of last thermotectonic event	USGS (1997)
Basin type	TOTAL
Rift type (for young rifts)	Şengör & Natal'in (2001)
Distances to feature	
Distance to ridge	UTIG (Plates project)
Distance to trench	UTIG (Plates project)
Distance to transform zone	UTIG (Plates project)
Distance to young rift	Şengör & Natal'in (2001)
Mean distance to 5 volcanoes	Siebert & Simkin (2002)

compiled by us from internal and external private databases and literature exploration, or derived from published global geophysical models. Below we give a detailed description of the source data and of how we derived the different proxies. We also discuss for each of them the relation to the thermal regime of the lithosphere, and the non-thermal components it is also likely to contain. We loosely grouped and sorted the observables in function of their relevance to the different components of surface heat flow, that is, crustal, mantle and integrated or geodynamics related component.

2.2.1 Heat production

In stable continental domains, the crustal heat production component is estimated to account for 20–80 per cent of the surface heat flow (Pollack & Chapman 1977; Rudnick & Fountain 1995; Artemieva & Mooney 2001). Unfortunately, in most regions, the precise distribution of radiogenic elements within the crust is poorly known, and only at the surface there are good-quality heat production determinations. The heat production A is normally obtained from the abundance of three radioactive elements, Uranium, Thorium and Potassium, according to the following formula:

$$A[\mu W\, m^{-3}] = 10^{-5}\rho\,(9.52C_{\rm U} + 2.56C_{\rm Th} + 3.48C_{\rm K})\,, \qquad (1)$$

where ρ is the rock density (kg m^{-3}) and $C_{\rm U}$ (ppm), $C_{\rm Th}$ (ppm) and $C_{\rm K}$ (per cent) are the radioactivity element content (Birch 1954; Rybach 1986). We computed and compiled surface heat production from various publicly available data sources, such as the IHFC database (Pollack *et al.* 1993), OZCHEM in Australia, LITO in Norway and GEOROC for Archean cratons. We also obtained an internal database from the French BRGM (Bureau des Recherches Géologiques et Minières), which compiled a large number of worldwide references (D. Thieblemont, personal communication), and detailed heat production analysis for different boreholes in Canada from UQAM (Université du Québec à Montréal) (J.-C. Mareschal, personal communication, 2008).

We then built up two observables from the merged data sets to get a representative global distribution on our $1^\circ \times 1^\circ$ grid. First, we attributed the median value of surface heat production to each grid cell containing heat production data (Fig. 3a). Because this observable does not cover a large percentage of the Earth's surface, we additionally opted for a second observable where the mean heat production is extrapolated over homogeneous continental provinces (Fig. 3b). The extrapolation is based on a division in 226 continental heat production provinces that were built up by combining major geological provinces (excluding large igneous province; LIPs) and thermotectonic age maps, mostly from the USGS (see Section 2.2.6), and that were successively generalized and completed with regional heat production information for uncovered regions (e.g. Sayan-Altai region; Puzankov *et al.* 1989). Of course, the so-defined provinces are likely to contain subelements formed in different environments, and as such they do not account for all the variability in heat production induced by the complexity of crustal assemblages. However, we believe that they are able to capture the large-scale trends of surface heat production, and thus may help recover some of the variations in surface heat flow.

2.2.2 Thickness of upper and middle crust

The thickness of the upper and middle crust may further help constrain the radiogenic contribution to surface heat flow, since most of the radiogenic contribution generally comes from those sections of the crust (Rudnick & Fountain 1995). Obviously, the precise distribution must be known to quantify the radiogenic heat flow component; but as a crude approximation, one may assume that it will generally be larger in a thicker upper/middle crust with the same geological affinity. We thus integrated the thicknesses of the upper and middle layers of the crust from the $2^\circ \times 2^\circ$ CRUST2.0 model (Bassin *et al.* 2000) (Figs 3c–d).

2.2.3 Upper-mantle density anomalies

Density of the lithospheric mantle is strongly controlled by the temperature variations in the mantle. Although it also carries a significant signal related to compositional differences between cratonic and non-cratonic mantle (e.g. Forte & Perry 2000; Kaban *et al.* 2003; Simmons *et al.* 2009), it should partly capture the variations of the thermal structure of the lithosphere. We thus adopted the $1^\circ \times 1^\circ$ mantle density grid of Kaban *et al.* (2004), which was derived globally by performing a long-wavelength isostatic adjustment of the densities on observed gravity, starting with an *a priori* model based on CRUST2.0 (Fig. 3e). Kaban *et al.* (2004) also estimated crustal density anomalies, which we did not integrate in this work, because the compositional component is likely to account for most of the variations.

2.2.4 Upper-mantle velocity structure

Similarly to mantle densities, variations in seismic velocities of the mantle are controlled by both the temperature field and compositional heterogeneities, the relative contribution of which is a matter of debate (e.g. Goes *et al.* 2000; Artemieva *et al.* 2004; Artemieva 2009, and previous refs). This indicates that velocity models of the upper mantle may give insight into the mantle component of heat flow. Because of the uncertainties related to the tomographic models, to the velocity–temperature relationship and to the compositional variations, it is not possible to directly estimate mantle heat flow from depth–velocity profiles converted to geotherms; we therefore decided to cluster a shear wave velocity model of the upper mantle (Shapiro & Ritzwoller 2002), obtained by surface wave tomography, into six continental and six oceanic classes of similar velocity structure (Fig. 3f). This was achieved by applying the k-means clustering algorithm (Forgy 1965)—the goal of which is to minimize iteratively the total intraclass variance—using the Euclidean distance between two velocity profiles $v_1(z)$, $v_2(z)$.

$$d^2\,(v_1, v_2) = \frac{\int_I w\,(z)\,[v_2(z) - v_1(z)]^2\,{\rm d}z}{\int_I w\,(z)\,{\rm d}z}. \qquad (2)$$

The integration is performed over the lithospheric mantle, $I =$ [20, 150 km] in oceanic domain and [50, 300 km] in continental domain, and the weighting function $w(z)$ decreases linearly from 1 to 0.4 between 100 km and 300 km depth to account for the deterioration of the model resolution with depth. Such a clustering has the advantage of being relatively independent of the selected velocity model, as suggest tests we carried out on some other models [SAW642AN, Panning & Romanowicz (2006); S362ANI, Kustowski *et al.* (2008)].

The 12 tomographic classes are believed to represent well-defined thermal regimes in the upper mantle and are as such added to our list of observables. As can be expected, there is a striking resemblance between these classes and the map of mean heat flow of Shapiro & Ritzwoller (2004) (Fig. 1c).

2.2.5 Topography

Within isostatically compensated regions, topography reflects the depth-integrated density of the lithosphere, which itself depends on temperature (but also on composition, see discussion earlier). We thus derived the mean topography on our $1^\circ \times 1^\circ$ grid from the ETOPO-2 raster data set supplied by the National Oceanic and Atmospheric Administration (NOAA 2006) (Fig. 3g).

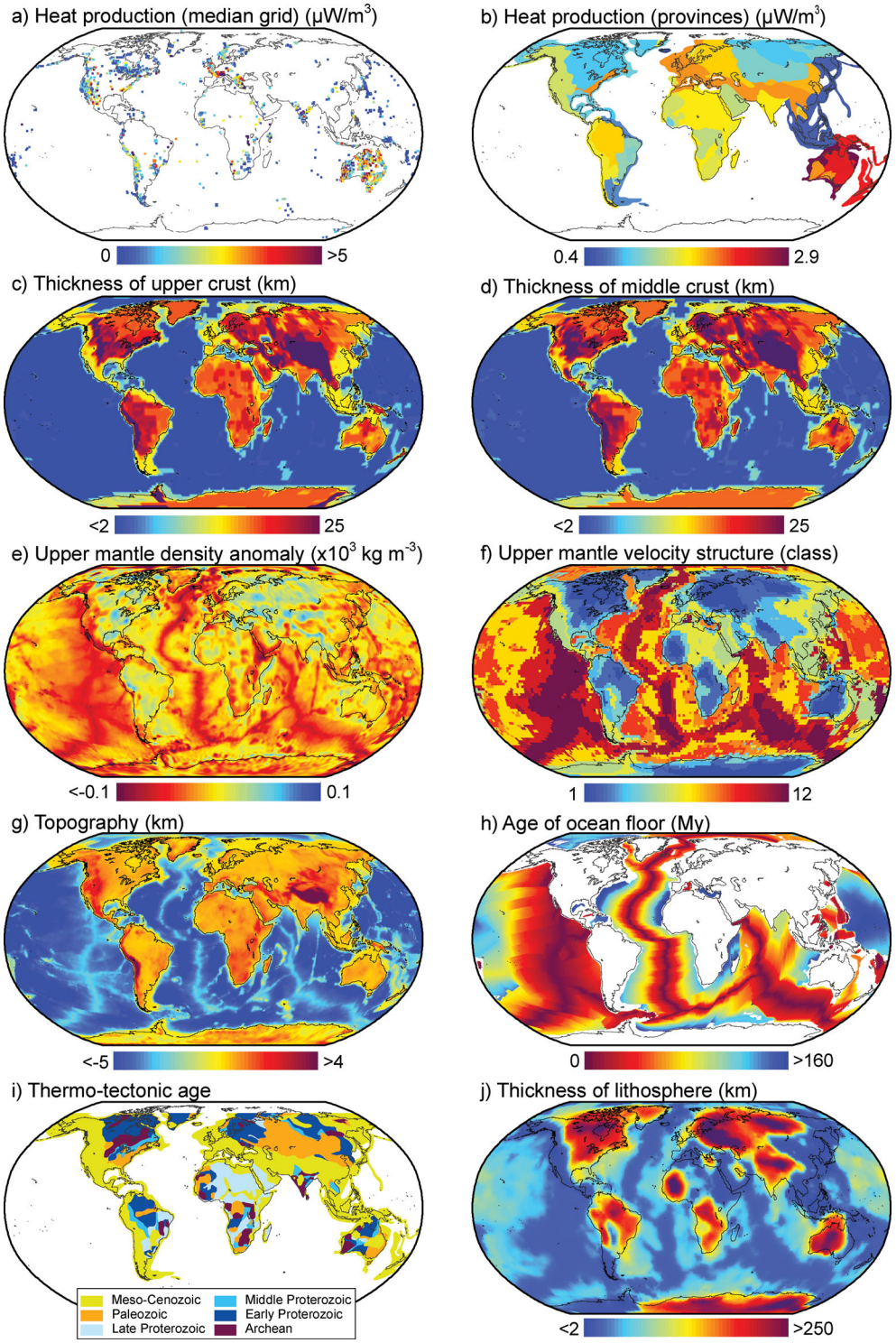

Figure 3. Terrestrial features used to build-up the observables incorporated in the extrapolation methods (see Table 1 and online supplementary material). Cells of the heat production grid are slightly exaggerated for clarity. See the electronic edition of the Journal for a colour version of this figure.

2.2.6 Age, thickness and geometry of the lithosphere

As stated in the Introduction, surface heat flow has been related to the age of the lithosphere, both in oceans and continents. The thermal evolution of oceanic lithosphere can be approximated as a 1-D conductive cooling, in which depth–temperature profiles depend mostly on the age of ocean floor (Parsons & Sclater 1977; Stein & Stein 1992). The relation should be understood statistically as a mean thermal structure for 'normal' oceans, though, from which significant regions may depart. Still, the age of oceanic lithosphere

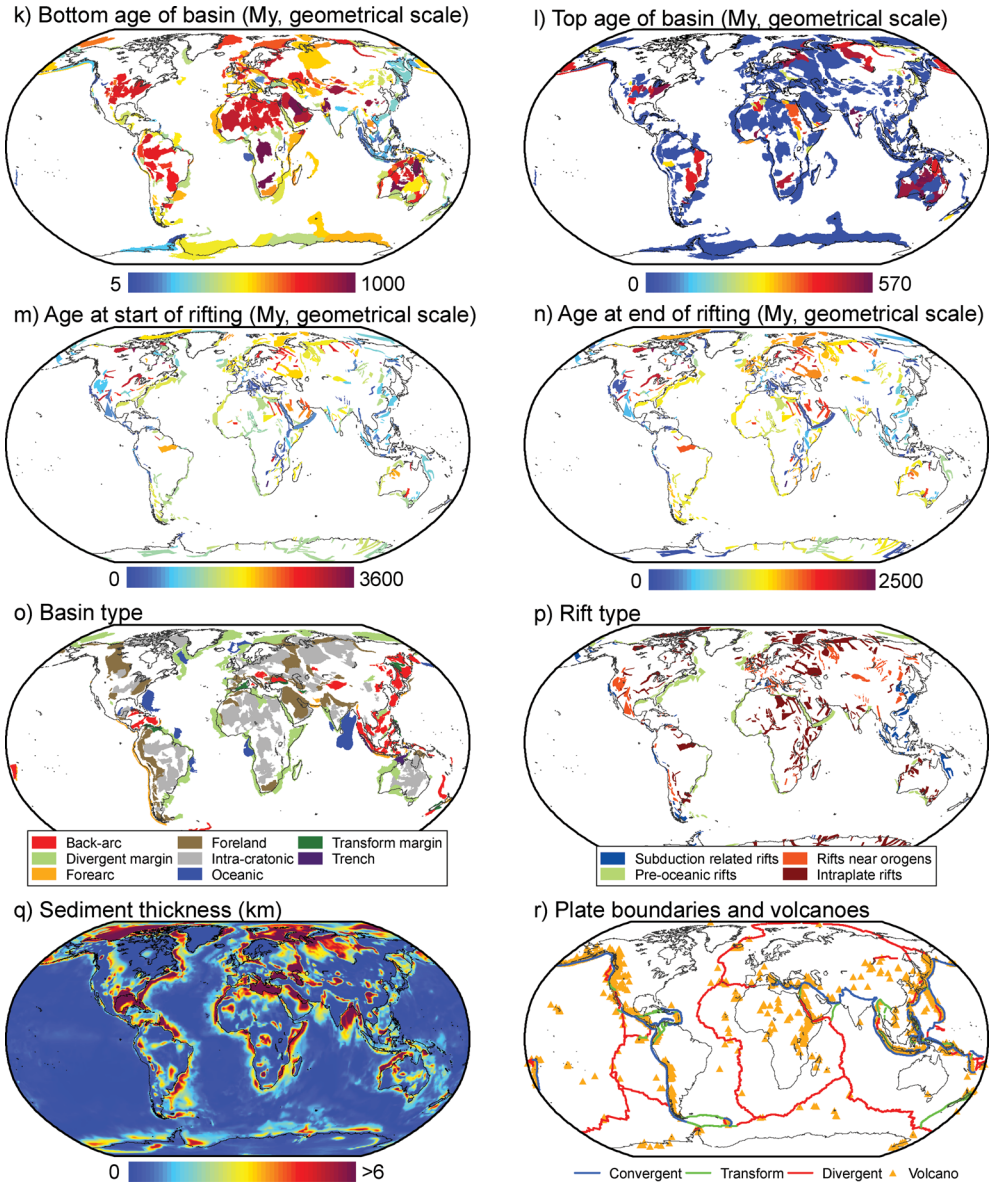

Figure 3. (*Continued.*)

is strongly related to its thermal structure, and we consequently added to the proxies the recently published 2′ × 2′ age grid of Müller *et al.* (2008), which was derived via interpolation of seafloor isochrones (Fig. 3h).

On continental lithosphere, there is a general trend of decreasing heat flow with increasing thermotectonic age (Vitorello & Pollack 1980), even though the relation is weak (Rao *et al.* 1982; Morgan 1984; Jaupart & Mareschal 2007). We used the global map of 'Thermo-Tectonic Age' published online by the U.S. Geological Survey (USGS) in 1997: it describes six age categories, from Meso- and Cenozoic to Archean (Fig. 3i), which were included as a class observable.

The thermal thickness of the lithosphere is obviously linked to its thermal structure, as it corresponds to the intersection of the conductive geotherm with the mantle adiabat. As such, it mostly reflects the mantle heat flow, but it is also sensitive to the exact depth distribution of crustal heat producing elements. We used seismic velocity anomalies as an indicator for the variations of the thermal thickness, even though differences may exist between the two (Artemieva 2009). To keep consistency with the classes of velocity structure (Section 2.2.4), we defined the base of the lithosphere from the shear velocity model of Shapiro & Ritzwoller (2002), as the depth of 2.5 per cent anomaly with respect to the reference model 'ak135' (Kennett *et al.* 1995) (Fig. 3j). Then, the gradient of the so-defined base was included as an additional observable, since lateral variations of the lithospheric thickness may generate a form of small-scale convection (Keen & Boutilier 1995; King & Anderson 1995), which can potentially affect heat transfers at the base of the lithosphere.

2.2.7 Basins, rifts and sediment thickness

The processes of formation of sedimentary basins and continental rifts imply lithospheric deformations by compression, extension or strike-slip tectonics. How the geotherm is affected depends on the type and timing of the deformations, and the possible subsequent thermal subsidence: an example of thermal evolution in an extensional environment is given by McKenzie (1978). The infill of

sediments itself affects heat flow through a permanent radiogenic heat component and a transient sedimentation effect.

To incorporate these contributions, we retrieved global information on sediment thickness, and on the classification and age of basins and rifts. The sources are the following: (1) the global grid of sediment thickness published by Laske & Masters (1997); (2) a world map of sedimentary basins provided by TOTAL, including top and bottom age of infill and basin classifications; and (3) the compilation of rifts of Şengör & Natal'in (2001), also including the age and type of rifting (Figs 3k–q). The class observable for the basins is based on a tectonic setting classification with the following typology defined: (1) backarc, (2) divergent margin, (3) forearc, (4) foreland, (5) intracratonic, (6) oceanic, (7) transform margin and (8) trench. The classification of the continental rifts involves the following categories: (1) intraplate rift, (2) pre-oceanic rift, (3) rift near orogen and (4) subduction-related rift. We also included the distance to the nearest active rift system (i.e. younger than 65 Ma).

2.2.8 Plate boundaries and volcanoes

Plate boundaries are zones of lithosphere creation or recycling, which are processes that alter the geotherm. The University of Texas Institute for Geophysics (UTIG) provides a compilation of plate boundaries, which are classified into (1) ridges, (2) trenches and (3) transforms (Fig. 3r). The observables derived from this data set are then the distances to each type of boundary.

Regional volcanism obviously indicates anomalous thermal conditions, and magmatic processes can further affect the surface geotherm and surface heat flow. We consequently integrated the global database of volcanoes of the Smithsonian Institution (Siebert & Simkin 2002), and derived from it the mean distance to the closest five volcanoes to minimize the effect of isolated volcanism on the predictions (Fig. 3r). We did not differentiate hotspot volcanism, because there is considerable uncertainty on the actual list and origin of hotspots (e.g. Courtillot *et al.* 2003; Anderson & Schramm 2005).

3 POSSIBLE APPROACHES OF GLOBAL HEAT FLOW EXTRAPOLATION

We now have at hand a set of imperfect proxies, which each contain partial information on the thermal state of the lithosphere. Since each proxy is weakly related to surface heat flow, one should find a way to extract the thermal component from all available information, rather than from a single estimator. (This is a situation which bears some resemblance to the problem of palaeoclimatic reconstruction.) We illustrate how the set of estimators may be used, in conjunction with the heat flow data, to infer heat flow distributions over the Earth. The first step consists in building up a set of examples on a global $1^\circ \times 1^\circ$ grid, by associating heat flow data with the corresponding observables, described in the previous section (Fig. 4). We can think of two simple approaches to associate a heat flow distribution with a given target point, owning a number of the selected observables. The best combination method explores combinations of observables and selects one of them that minimizes the dispersion of the generated heat flow distribution (Fig. 4, left-hand side). The latter distribution is defined as the subset of examples whose observables belonging to the combination are similar to those of the target point. The similarity method uses all the available observables and affects a weight to each example, depending on the degree of similarity between the target point and the example (Fig. 4, right-hand side). The degree of similarity is arbitrarily defined as the number of similar observables between the target and the example. The obtained heat flow distribution can be interpreted as a probability distribution for the heat flow value at

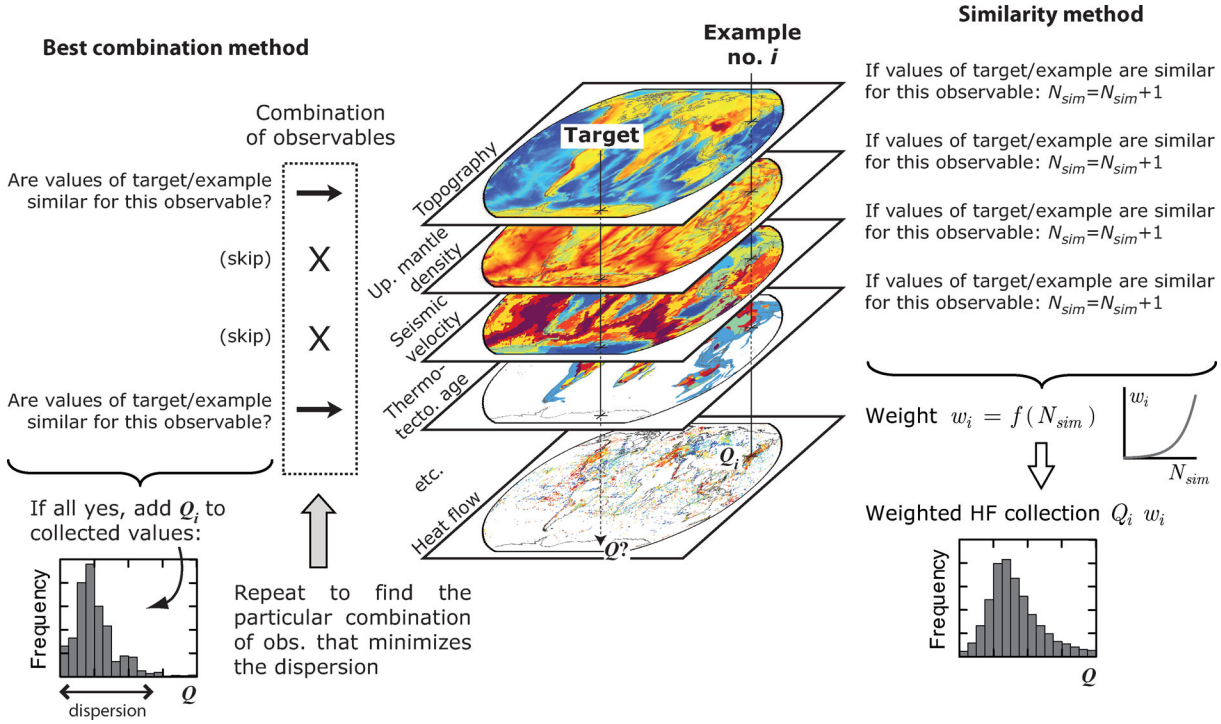

Figure 4. Suggested approaches to associate a heat flow distribution with any target point (see text for details). See the electronic edition of the Journal for a colour version of this figure.

the target point. The similarity method is in many ways comparable to the method of Shapiro & Ritzwoller (2004), who used a seismic model to guide the extrapolation of heat flow based on a structural similarity functional.

Formally, for every $1^\circ \times 1^\circ$ cell on which a heat flow value Q_i exists, Q_i was grouped with the corresponding N observables X_i^j ($j = 1 \dots N$) previously built up to form an example vector $\mathbf{X}_i = [X_i^1 \dots X_i^N \; Q_i]$. The problem then consists in associating a heat flow distribution with any new vector of observables' values $\mathbf{Y} = [Y^1 \dots Y^N]$, normally derived from a cell with no heat flow defined, using the set of examples $\{\mathbf{X}_1, \mathbf{X}_2, \mathbf{X}_3 \dots\}$. Note that within an example vector $\mathbf{X}_i$ the heat flow value Q_i must be defined, but not necessarily all observables associated with it: indeed some features, such as median heat production or basin type, do not exist all over the grid.

We previously employed the term *similar* several times: two values X^j, Y^j of a given observable j are considered to be similar ($X^j \cong Y^j$) under a few conditions depending on the type of the observable, as described in the previous section. Both values must be of course defined. For a continuous observable, the values should be close enough:

$$X^j \cong Y^j \Leftrightarrow \left|Y^j - X^j\right| < \delta. \tag{3}$$

To account for scale differences between different observables, δ is defined as a fraction of the 95 per cent range of the observable's values. After some tries, we opted for $\delta =$ one twentieth of the latter range.

In the case of a class observable, taking on a finite number of values, X^j and Y^j must be strictly equal:

$$X^j \cong Y^j \Leftrightarrow X^j = Y^j. \tag{4}$$

Finally, observables that represent a distance to a feature are treated like continuous observables, except that a threshold distance D is introduced, since a given feature cannot affect heat flow over an infinite distance.

$$X^j \cong Y^j \Leftrightarrow \begin{cases} \left|Y^j - X^j\right| < \delta, \\ \text{and} |X^j|, |Y^j| < D. \end{cases} \tag{5}$$

Here we took $\delta = 50$ km, since smaller distances cannot be resolved on the $1^\circ \times 1^\circ$ grid we worked with. We then found that a threshold $D = 400$ km gave the best results to validation tests (see next section): such a value seems consistent with the physical intuition for the maximum distance over which a terrestrial feature is expected to exert some influence.

3.1 Best combination method

The idea of the best combination method is to seek the combination of observables that minimizes the dispersion of the generated heat flow distribution. Let $\mathbf{Y} = [Y^1 \dots Y^N]$ be the values of the observables at the target point. For any subset $\mathcal{S}$ of the observables ($\mathcal{S} \subset \{1 \dots N\}$), a distribution of heat flow $Q(\mathcal{S})$ can be formed by keeping the examples $\mathbf{X}_i$ such that all values of $\mathbf{X}_i$ and $\mathbf{Y}$ belonging to the subset $\mathcal{S}$ are similar:

$$Q(\mathcal{S}) = \left\{ Q_i \text{ from } \mathbf{X}_i \text{ such that} X_i^j \cong Y^j, \text{ for } j \in \mathcal{S} \right\}. \tag{6}$$

Statistical measures may be derived from this distribution, such as the number of elements $\mathcal{N}_{Q(\mathcal{S})}$, the mean $\overline{Q}(\mathcal{S})$, the standard deviation $\sigma_{Q(\mathcal{S})}$ and the coefficient of variation $\sigma_{Q(\mathcal{S})}/\overline{Q}(\mathcal{S})$. We chose to minimize the latter measure of dispersion rather than the standard deviation, because it is preferable the use a dimensionless measure not to bias the extrapolation towards low, less dispersed heat flow values. Also, the distribution must be large enough to be meaningful. Hence we formally seek the particular subset of observables $\hat{\mathcal{S}}$ such that

$$\mathcal{N}_{Q(\hat{\mathcal{S}})} > N_{\min} \quad \text{and} \quad \frac{\sigma_{Q(\hat{\mathcal{S}})}}{\overline{Q}(\hat{\mathcal{S}})} \text{ minimum.} \tag{7}$$

From a practical viewpoint, it is computationally expensive to explore all possible combinations, so we restricted the investigation to subsets with a maximum of three observables. $\hat{\mathcal{S}}$ is interpreted as the most relevant set of observables for the target configuration $\mathbf{Y}$, as it yields the most homogeneous heat flow distribution. This particular distribution $Q(\hat{\mathcal{S}})$ is the one associated with $\mathbf{Y}$.

3.2 Similarity method

The similarity method takes on a more classical approach in which each example $\mathbf{X}_i$ is given a certain weight w_i, depending on its degree of similarity with the target configuration $\mathbf{Y}$. We define the degree of similarity between $\mathbf{X}_i$ and $\mathbf{Y}$ as their number of similar values:

$$N_{\text{sim}}(\mathbf{X}_i, \mathbf{Y}) = \text{Count of} X_i^j \cong Y^j, \text{ for} j = 1 \dots N. \tag{8}$$

The weight w_i is affected to $\mathbf{X}_i$ through a weighting function f that must increase sharply with the degree of similarity. After a several tries we selected exponentially growing functions:

$$w_i = f(N_{\text{sim}}(\mathbf{X}_i, \mathbf{Y})) \quad \text{with } f(N_{\text{sim}}) = K^{N_{\text{sim}}}, \tag{9}$$

meaning that each supplementary unit of degree of similarity yields a multiplication of the weight by K. The particular case $K =$ e corresponds to the exponential function.

The obtained collection of weighted heat flow values Q_i, w_i associated with $\mathbf{Y}$ is characterized by classical statistical measures such as the mean and the standard deviation.

$$\overline{Q} = \frac{\sum_i w_i Q_i}{\sum_i w_i}, \tag{10}$$

$$\sigma_Q = \sqrt{\frac{\sum w_i \left(Q_i - \overline{Q}\right)^2}{\sum w_i}}. \tag{11}$$

The procedure is illustrated in Fig. 5, for two target points located in Antarctica, where no measurement exists. We find, like Shapiro & Ritzwoller (2004), that eastern Antarctica is highly similar to tectonically stable areas (East European Craton, North American Craton, Indian Shield, South African Craton and western Australian cratons), while the western part is more similar to extensional regions (western North America, Red Sea, East China Sea and Sea of Japan), which is consistent with the tectonics of Antarctica (e.g. Dalziel & Elliot 1982; Behrendt 1999). As a result, the heat flow distribution associated with the latter point has markedly higher mean and dispersion.

4 DISCUSSION

The average and dispersion of the heat flow distributions obtained from both suggested methods are presented in Fig. 6 and in the online supplementary material. These heat flow maps are the result of an optimization procedure for both methods that consisted in adjusting the intrinsic parameters and in choosing a compromise grid for the heat flow examples. The accuracy was evaluated by comparing the predicted distribution with the heat flow examples directly and

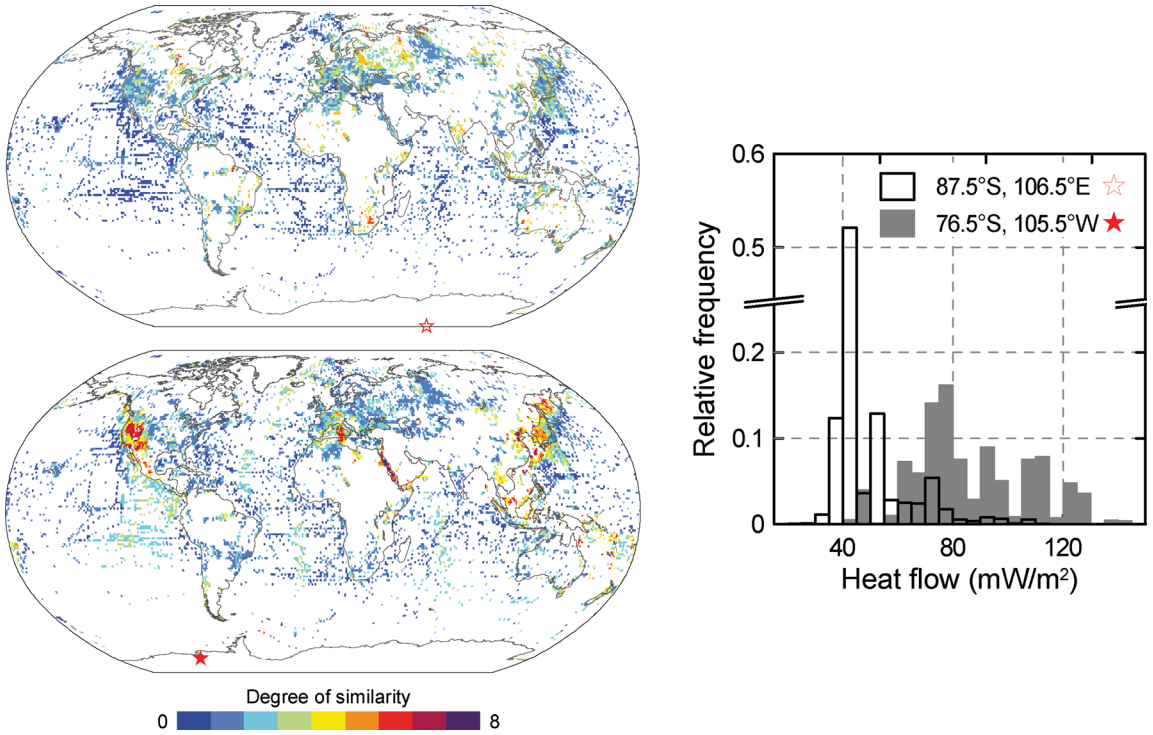

Figure 5. Similarity of the examples with a target point located in eastern Antarctica (top panel) and another in western Antarctica (bottom panel), represented by the stars. The associated heat flow distributions were obtained using a weight function $w_i = 10^{N_{\mathrm{sim}}}$, and a grid of heat flow examples smoothed with a 500 km radius Gaussian filter (see Section 2.1). The maximum degree of similarity is much lower than the total number of proxies because many of them are not available in Antarctica. See the electronic edition of the Journal for a colour version of this figure.

through validation tests discussed below. For the best combination method we imposed a minimum of examples per distribution $N_{\mathrm{min}} = 40$, while for the similarity method the best results were obtained used a weight function $w_i = 10^{N_{\mathrm{sim}}}$.

The trends of the mean heat flow produced by both methods are similar. The lowest values (30–50 mW m^{-2}) appear inside and around the Archean and Palaeoproterozoic nuclei (e.g. East European Craton, Siberian Craton, Amazonian Shield, West African Craton), which are depleted in heat producing elements. Broad areas of high heat flow (>70 mW m^{-2}) are outlined along spreading centres, active orogens (Alpine–Himalayan and Circum–Pacific belt), active rifts (East African Rift and Gulf of Aden) and zones associated with high crustal concentrations of heat producing elements and/or mantle plume heating (western Europe, Sahara). Also, the extrapolations reveal a marked polarity within Antarctica, between the tectonically active western part and stable eastern part (70–80 mW m^{-2} vs. ∼50 mW m^{-2}), as previously inferred by Shapiro & Ritzwoller (2004).

The standard deviations of the best combination method are globally lower than those of the similarity method, because the former method seeks to minimize the dispersion of the distributions. Actually, the measures of dispersion produced by the similarity method may better characterize the local variability and intrinsic uncertainty of heat flow. In any case, the trends of the standard deviation of both methods are consistent with the tectonic context: the highest dispersions are found near oceanic ridges, reflecting the effect of hydrothermal activity on surface heat flow, and generally low dispersions appear in Archean cratons, where the globally low radiogenic component yield worldwide homogeneous values. The best combination and similarity methods yield a mean continental heat flow of about 62 mW m^{-2} and 63.6 mW m^{-2}, respectively, corresponding to a continental heat loss of 13.2 ± 0.6 TW and 13.6 ± 0.8 TW. (The reported errors correspond to the 2-sigma uncertainties of the continental heat loss, which were estimated from the standard deviations of the predicted distributions, taking into account the spatial autocorrelation of the errors.) Those results are in agreement with previous estimates, which are in the range 13–14 TW (Pollack *et al.* 1993; Jaupart *et al.* 2007; Davies & Davies 2010). The problem of conductive heat loss through the ocean floor is not discussed here, since heat flow measurements (and consequently also the values derived from our statistical approaches) contain an advective component due to hydrothermal circulation which occurs in Cenozoic oceanic crust (Stein & Stein 1994, and references therein): as a consequence, conductive models rather than measurements are usually used to estimate the oceanic power loss (e.g. Pollack *et al.* 1993).

We pointed out in the introduction the existence of previous efforts of heat flow extrapolation, using basic interpolation methods or a few geological or geophysical estimators (e.g. Chapman & Pollack 1975; Pollack *et al.* 1993; Shapiro & Ritzwoller 2004; Davies & Davies 2010). The guiding concepts of our similarity method are close to those employed by Shapiro & Ritzwoller (2004), who assigned heat flow distributions to target points on the basis of a seismic velocity model of the crust and upper mantle. A comparison of their results with the mean heat flow produced by the similarity method is shown in Fig. 7 . The latter method shows the same general heat flow trends, but produces in general additional smaller wavelength anomalies. Some important differences are noted in both continents and oceans. Stronger regional thermal highs are affected to, for example, central Australia and the northern Cordillera. Lower heat flow appears in Arabia, the Himalaya and many parts of Asia. The broad area of high heat flow in the Sahara has a slightly different shape, more confined to the north-

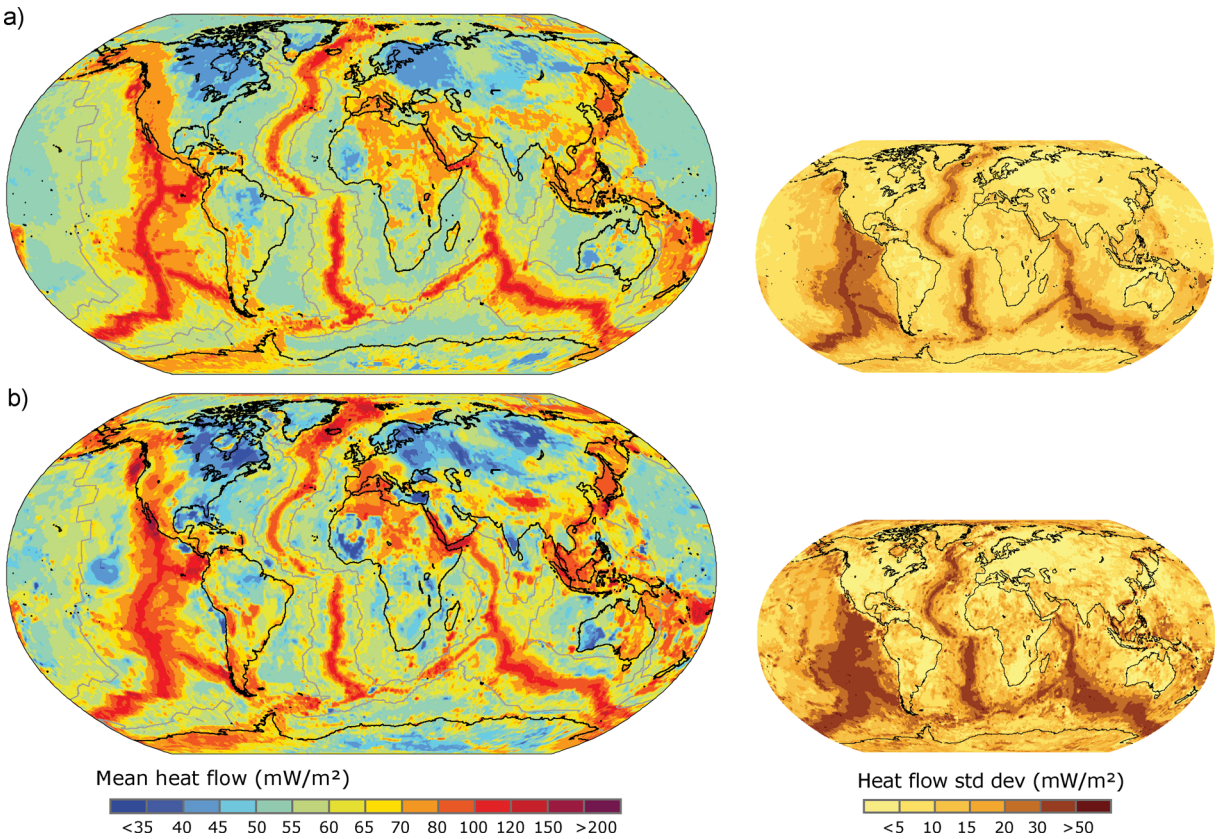

Figure 6. Global heat flow maps obtained from (a) the best combination method and (b) the similarity method: mean value (left-hand side) and standard deviation (right-hand side) of the distributions. Grey lines show the 60 Myr contour of seafloor age (Müller *et al.* 2008) [heat flow is likely to contain a systematic advective component below such an age (e.g. Stein & Stein 1994)]. A Gaussian filter with a 500 km radius was applied to the grid of heat flow examples (see Section 2.1). The minimum number of examples per distribution of the best combination method was set to $N_{\min} = 40$ and the weight function of the similarity method was defined as $w_i = 10^{N_{\text{sim}}}$. The lower standard deviations of the best combination method do not imply a better accuracy, but rather reflect the intrinsic procedure of the method (see Section 4). Data are available in the online supplementary material. See the electronic edition of the Journal for a colour version of this figure.

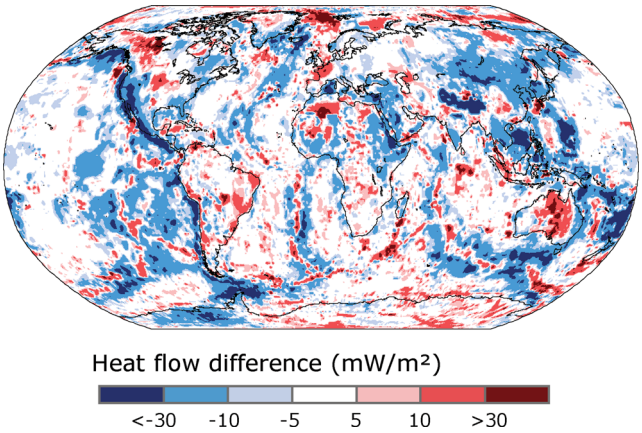

Figure 7. Difference between the mean heat flow produced by the similarity method (Fig. 6b) and that of Shapiro & Ritzwoller (2004) (Fig. 1c). Positive differences correspond to higher heat flow for our similarity method. See the electronic edition of the Journal for a colour version of this figure.

ern Sahara and extending to the west in Algeria and Morocco. The thermal anomaly associated with the Red Sea Rift and East African Rift does not extend beyond the rift system. As for Antarctica, the marked polarity between the eastern and the western part also appears, but the heat flow difference is not as strong as in Shapiro & Ritzwoller (2004). In the oceans, their map shows a smoother heat flow decrease with age, but anyway both our method and theirs are biased by the effect of hydrothermal circulation in young oceanic crust. In any case, the conductive heat flow in young oceans should be inferred using a conductive thermal model, such as the plate model (Parsons & Sclater 1977; Stein & Stein 1992) or the Chablis model (Crough 1975; Doin & Fleitout 1996), rather than direct measurements.

4.1 Cross-validation statistics

To assess the accuracy of the methods, a leave-one-out cross-validation procedure was followed: the procedure consisted in (1) setting aside one $1^\circ \times 1^\circ$ cell, and all data within a radius of 1000 km, from the set of examples, (2) comparing the heat flow value of that test cell with the output of the methods and (3) repeating this for all examples. The exclusion radius of 1000 km around each cell is well above the intrinsic correlation distance of heat flow (Fig. 2) and the diameter of the Gaussian filters applied to heat flow (Table 2), which ensures that cross-validation statistics are not artificially improved by the effect of spatial autocorrelation. Such statistics implied comparing scalar values (heat flow set aside) with distributions (output of the methods), which was achieved by computing weighted quantities between the values set aside and the mean of the predicted distributions, using weights inversely proportional to the variance of the distributions. The case of methods having

Table 2. Summary of the cross-validation statistics, weighted by the inverse of distributions' variance. R_{filter}: radius of the Gaussian filter applied to the heat flow grid [=3 times the conventional Gaussian sigma, see command `grdfilter` from the Generic Mapping Tools (Wessel & Smith 1991)]; MARD: mean absolute relative deviation (per cent); RMSD: root mean square deviation (mW m^{-2}); r: coefficient of correlation.

	Best comb. method				Similarity method			
R_{filter}	MARD (per cent)	RMSD	r	r^2	MARD (per cent)	RMSD	r	r^2
Continents								
–	31.4	24.8	0.25	0.06	33.3	24.7	0.34	0.11
200 km	25.3	19.8	0.32	0.10	22.9	17.7	0.61	0.37
350 km	21.5	16.5	0.40	0.16	17.2	13.4	0.67	0.45
500 km	19.5	14.9	0.45	0.20	13.9	11.6	0.77	0.59
Oceans								
–	49.1	32.5	0.25	0.06	45.7	29.0	0.21	0.04
200 km	36.3	27.0	0.31	0.09	32.9	24.0	0.32	0.10
350 km	24.7	21.7	0.38	0.14	23.7	19.8	0.45	0.19
500 km	19.5	18.5	0.42	0.18	19.5	17.1	0.48	0.23

no predictive skill corresponds to a cross-validation correlation coefficient close to zero, and an rms error greater than the standard deviation of heat flow examples (>20 mW m^{-2} on continents, >40 mW m^{-2} on oceans; see Fig. 2).

As shown in Table 2, validation statistics are systematically better on continents than on oceans, which is largely due to the high variability of surface heat flow on oceanic ridges, itself the consequence of hydrothermal circulation. Although the trends uncovered by both methods are similar, continental predictions of the similarity method are more accurate than those of the best combination method, and the difference in accuracy between the methods gets more important as the width of the Gaussian filter applied on heat flow increases. The coefficient of determination r^2 is low when unsmoothed heat flow examples are used, which shows that short-scale variations of heat flow are poorly resolved. Such a result is to be expected, because the prediction accuracy of shortest scale trends is hampered by the lack of detailed resolution of fundamental components such as the radiogenic heat production. However, the similarity method possesses significant skill in retrieving medium- to large-scale variations, as its continental r^2 and rms error approach 0.6 and 10 mW m^{-2}, respectively, after removing features of wavelength shorter than 500–1000 km from heat flow data (Table 2). As explained earlier, the better results of validation statistics on longer wavelengths are not mere artefacts due to the autocorrelation introduced by spatial smoothing: this really means that the selected proxies have the potential to retrieve a part of the medium-scale features of surface heat flow.

4.2 Predictive power of the proxies

Finally, the predictive power of a given proxy can be assessed by calculating the degradation of cross-validation statistics after the proxy has been removed from the list presented in Table 1. Such a test should not be overinterpreted, though, because its results depend on several parameters, such as the initial set of proxies, the selected method, its intrinsic parameters and, of course, the statistics considered. Nevertheless, Fig. 8 qualitatively shows that, on continents, the proxies that exert the strongest influence on the predictions' accuracy are related to the trends in crustal radiogenic contribution, to the integrated thermal structure (topography, thickness of the lithosphere) and to the geodynamic transient component (rifts, basins and volcanism). Although the latter component concerns limited areas of the lithosphere, it is likely to cause locally strong variations of heat flow, which explains its relative importance in the predictions.

On oceans, accuracy is unsurprisingly controlled by proxies whose variations depend on the age of ocean floor (oceanic age itself, velocity structure, mantle density and topography). The coefficient of determination r^2 is also sensitive to proxies related to rifts and trenches, because they can help retrieve extreme values on newly oceanized rifts (e.g. Gulf of Aden) or subduction zones. However, we note that none of the proxies exert a significant influence on oceanic r^2, because of the fundamentally unpredictable nature of surface heat flow variations within young oceanic crust.

4.3 Advantages and limitations

Both new methods of extrapolation estimate the heat flow in each target point from a heat flow distribution, rather than defining a deterministic value. This creates smoothed global heat flow maps, where the dispersion measures such as the standard deviation can help to characterize the short-scale variability and the intrinsic uncertainty of heat flow. The approaches are designed to handle incomplete sets of observables, which allows including features that are not known or relevant over the whole planet, such as heat production and basin type. The methods and validation statistics are rather rudimentary in nature, and contain several *ad hoc* adjustments such as the weight function or the threshold distance. They nevertheless illustrate how surface heat flow may be extracted from various imperfect proxies, each partly (and mostly, weakly) related to the thermal state of the lithosphere. Validation tests are encouraging, and suggest that the proxies have the potential to retrieve part of the medium-scale heat flow variations.

Of course, the empiric nature of the approaches limits their accuracy, since the outcome is strongly depending on the quality of the heat flow examples and guiding data sets; biased heat flow data will also be extrapolated. This is reflected in particular in the oceans, where heat flow data in young oceanic crust are limited to well-sedimented areas, which are strongly disturbed by fluid recharge processes reducing the surface heat flow values (Stein & Stein 1994; Elderfield *et al.* 2004). More generally, the methods possess the advantages and disadvantages of empiricism: they allow one to extrapolate quickly heat flow by simple transposition of existing measurements in regions of similar geodynamic context, but they rely on the assumption that heat flow data already cover the whole variety of present-day geodynamics, and of course

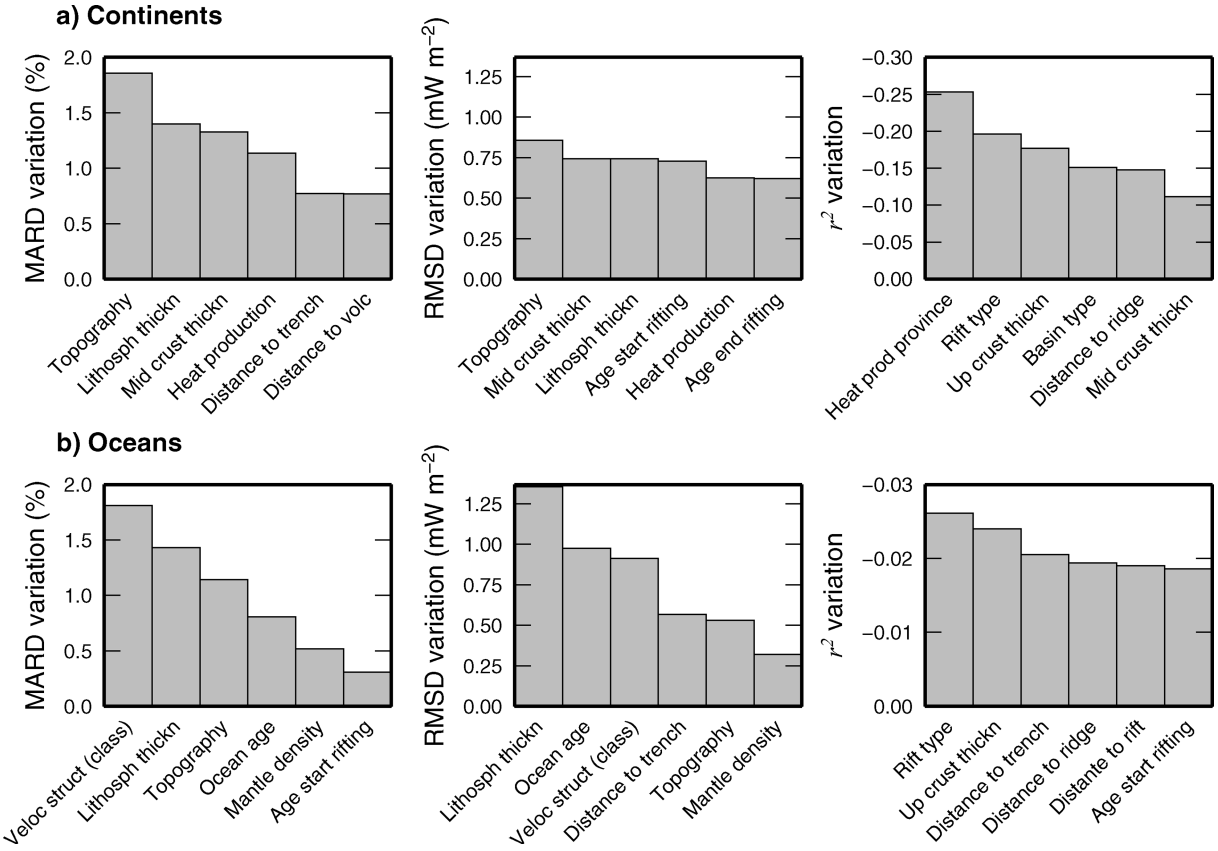

Figure 8. Variation in cross-validation statistics after removing a given proxy from the set of Table 1. The plots show the proxies whose removal causes the strongest degradations. We used the similarity method, with a weighting function $w_i = 10^{N_{\text{sim}}}$ and a 500 km radius Gaussian filter applied to the heat flow examples.

they do not provide a sound physical model of heat transfers in the lithosphere, nor they can replace actual measurements.

5 CONCLUSION

Unlike many geological and geophysical features, surface heat flow is unknown on large parts of the Earth. We thus introduced two empirical methods to extrapolate heat flow by transposition of existing measurements: the best combination and similarity methods. The basic idea is that similar geodynamic settings should display similar thermal states. Including a large set of estimators rather than a single one obviously allows to best represent the wide variety of geodynamic environments; this is why we selected several terrestrial proxies related to the thermal state of the lithosphere, including mantle seismic velocity, geodynamic setting, physical and tectonic parameters in the crust and sedimentation information at the surface. Each observable is partly related to one or several components of the heat flow at the surface. We tried to show how such an array of estimators may by used to assign a heat flow distribution to a given target point: either by weighting the examples as a function of their similarity with the target (similarity method); or by selecting the particular subset of estimators that minimizes the dispersion of the generated heat flow distribution on the target (best combination method).

The global maps of mean heat flow produced by both methods outline the general trends of low heat flow in tectonically stable and ancient regions, and thermal high in orogens and rift systems. A broad thermal anomaly is assigned to the Sahara, and a marked polarity appears within Antarctica, whose eastern part is expected to exhibit a high heat flow given its resemblance with many tectonically active regions of the world. The similarity method has an overall accuracy, as determined by validation tests, which is better than the best combination method. Those validation tests suggest that, although short-scale features of heat flow are poorly predicted, the proxies are able to retrieve a significant part of medium- to large-scale trends. The heat flow distributions offer details that may be valuable in practical applications, such as basin modelling. Moreover, the approaches could potentially be applied to extrapolate heat flow in the past, as palaeomaps exist or can be reconstructed for many of the observables. If one assumes that the present-day variety of geodynamic environments and associated thermal states are representative for the past too, then the present-day examples may be used in conjunction with palaeo-estimators to derive time reconstructions of the surface heat flow.

ACKNOWLEDGMENTS

This study was supported by a grant from Total. We are thankful to all the people that have helped us during the study by inspiring discussions and data and software contributions. In particular, we are indebted to D. Thieblemont (BRGM), J.-C. Mareschal (UQAM-IPGP), P. Patriat (IPGP), J. Besse, (IPGP), N. Shapiro (IPGP), F. Fluteau (IPGP) and P. Unternehr (TOTAL). Irina Artemieva and an

anonymous reviewer suggested significant improvements to the first version of the manuscript.

REFERENCES

Anderson, D.L. & Schramm, K.A., 2005. Global hotspot maps, in *Plates, Plumes and Paradigms,* pp. 19–29, eds Foulger, G.R., Natland, J.H., Presnall, D.C. & Anderson, D.L., Geological Society of America Special Paper 388, doi:10.1130/2005.2388(03).

Artemieva, I.M., 2009. The continental lithosphere: reconciling thermal, seismic, and petrologic data, *Lithos,* **109,** 23–46, doi:10.1016/j.lithos.2008.09.015.

Artemieva, I.M. & Mooney, W.D., 2001. Thermal thickness and evolution of precambrian lithosphere: a global study, *J. geophys. Res.,* **106**(B8), 16 387–16 414.

Artemieva, I.M., Billien, M., Lévêque, J.-J. & Mooney, W.D., 2004. Shear wave velocity, seismic attenuation, and thermal structure of the continental upper mantle, *Geophys. J. Int.,* **157,** 607–628, doi:10.1111/j.1365-246X.2004.02195.x.

Bassin, C., Laske, G. & Masters, G., 2000. The current limits of resolution for surface wave tomography in north america, *EOS, Trans. Am. geophys. Un.,* **81**(48), Fall Meet. Suppl., Abstract F897.

Behrendt, J.C., 1999. Crustal and lithospheric structure of the west antarctic rift system from geophysical investigations: a review, *Global planet. Change,* **23,** 25–44.

Birch, F., 1954. Heat from radioactivity, in *Nuclear Geology,* pp. 148–174, ed. Faul, H., Wiley & Sons, New York.

Chapman, D.S. & Pollack, H.N., 1975. Global heat flow: a new look, *Earth planet. Sci. Lett.,* **28,** 23–32.

Courtillot, V., Davaille, A., Besse, J. & Stock, J., 2003. Three distinct types of hotspots in the Earth's mantle, *Earth planet. Sci. Lett.,* **205,** 295–308.

Crough, S.T., 1975. Thermal model of oceanic lithosphere, *Nature,* **256,** 388–390.

Dalziel, I.W.D. & Elliot, D.H., 1982. West Antarctica: problem child of Gondwanaland, *Tectonics,* **1**(1), 3–19.

Davies, J.H. & Davies, D.R., 2010. Earth's surface heat flux, *Solid Earth,* **1**(1), 5–24, doi:10.5194/se-1-5-2010.

Davis, E.E. & Lister, C.R.B., 1974. Fundamentals of ridge-crest topography, *Earth planet. Sci. Lett.,* **21,** 405–413.

Doin, M.P. & Fleitout, L., 1996. Thermal evolution of the oceanic lithosphere: an alternative view, *Earth planet. Sci. Lett.,* **142,** 121–136.

Elderfield, H., Becker, K. & Davis, E.E., 2004. Foundations of research into heat, fluid, and chemical fluxes in oceanic crust, in *Hydrogeology of the Oceanic Lithosphere,* pp. 28–56, eds Davis, E.E. & Elderfield, H., Cambridge University Press, Cambridge.

Forgy, E., 1965. Cluster analysis of multivariate data: efficiency vs interpretability of classifications, *Biometrics,* **21,** 768–769.

Forte, A.M. & Perry, H.K.C., 2000. Geodynamic evidence for a chemically depleted continental tectosphere, *Science,* **290,** 1940–1944.

Goes, S., Govers, R. & Vacher, P., 2000. Shallow mantle temperatures under Europe from *P* and *S* wave tomography, *J. geophys. Res.,* **105**(B5), 11 153–11 169.

IHFC, 2009. The global heat flow database provided by the international heat flow commission (ihfc). Available at http://www.heatflow.und.edu, last updated June 10, 2009.

Jaupart, C. & Mareschal, J.C., 2007. Heat flow and thermal structure of the lithosphere, in *Treatise on Geophysics, Vol. 6: Crust and Lithosphere Dynamics,* pp. 217–251, ed. Watts, A.B., Elsevier, Amsterdam.

Jaupart, C., Labrosse, S. & Mareschal, J.C., 2007. Temperatures, heat and energy in the mantle of the earth, in *Treatise on Geophysics, Vol. 7: Mantle Convection,* pp. 253–303, ed. Bercovici, D., Elsevier, Amsterdam.

Kaban, M.K., Schwinter, P., Artemieva, I.M. & Mooney, W.D., 2003. Density of continental roots: compositional and thermal contributions, *Earth planet. Sci. Lett.,* **209,** 53–69, doi:10.1016/S0012-821X(03)00072-4.

Kaban, M.K., Schwintzer, P. & Reigber, C., 2004. A new isostatic model of the lithosphere and gravity field, *J. Geod.,* **78,** 368–385, doi:10.1007/s00190-004-0401-6.

Keen, C.E. & Boutilier, R.R., 1995. Lithosphere-asthenosphere interactions below rifts, in *Rifted Ocean-Continent Boundaries,* pp. 17–30, eds Banda, E., Torné, M. & Talwani, M., Kluwer, Dordrecht.

Kennett, B.L.N., Engdahl, E.R. & Buland, R., 1995. Constraints on seismic velocities in the Earth from traveltimes, *Geophys. J. Int.,* **122**(1), 108–124.

King, S.D. & Anderson, D.L., 1995. An alternative mechanism of flood basalt formation, *Earth planet. Sci. Lett.,* **136,** 269–279.

Kustowski, B., Ekström, G. & Dziewoński, A.M., 2008. Anisotropic shear-wave velocity structure of the Earth's mantle: a global model, *J. geophys. Res.,* **113,** B06306, doi:10.1029/2007JB005169.

Laske, G. & Masters, G., 1997. A global digital map of sediment thickness, *EOS, Trans. Am. geophys. Un.,* **78,** F483.

McKenzie, D., 1978. Some remarks on the development of sedimentary basins, *Earth planet. Sci. Lett.,* **40,** 25–32.

Morgan, P., 1984. The thermal structure and thermal evolution of the continental lithosphere, *Phys. Chem. Earth,* **15,** 107–185.

Müller, R.D., Sdrolias, M., Gaina, C. & Roest, W.R., 2008. Age, spreading rates, and spreading asymmetry of the world's ocean crust, *Geochim. Geophys. Geosyst.,* **9,** Q04006, doi:10.1029/2007GC001743.

NOAA, 2006. 2-minute Gridded Global Relief Data (ETOPO2v2), Tech. Rep., U.S. Department of Commerce, National Oceanic and Atmospheric Administration, National Geophysical Data Center, URL http://www.ngdc.noaa.gov/mgg/fliers/06mgg01.html (last accessed 2011 September 30).

Panning, M. & Romanowicz, B., 2006. A three-dimensional radially anisotropic model of shear velocity in the whole mantle, *Geophys. J. Int.,* **167,** 361–379, doi:10.1111/j.1365-246X.2006.03100.x.

Parsons, B. & Sclater, J.G., 1977. An analysis of the variation of ocean floor bathymetry and heat flow with age, *J. geophys. Res.,* **82**(5), 803–827.

Pollack, H.N. & Chapman, D.S., 1977. Mantle heat flow, *Earth planet. Sci. Lett.,* **34,** 174–184.

Pollack, H.N., Hurter, S.J. & Johnson, J.R., 1992. Global heat flow data set, Tech. rep., World Data Center A for Solid Earth Geophysics, NOAA E/GCI, 325 Broadway, Boulder, CO 80303, USA.

Pollack, H.N., Hurter, S.J. & Johnson, J.R., 1993. Heat flow from the Earth's interior: analysis of the global data set, *Rev. Geophys.,* **31,** 267–280.

Puzankov, Y.N., Duchkov, A.D., Melgunov, S.V. & Noshkin, A.D., 1989. *Radioactive Elements and Radiogenic Heat Generation in the Structural Complexes of Altai-Sayan Oblast,* Novosibirsk IGG-SBRAS, 158 p. (in Russian).

Rao, R.U.M., Rao, G.V. & Reddy, G.K., 1982. Age dependence of continental heat flow: fantasy and facts, *Earth planet. Sci. Lett.,* **59,** 288–302.

Rudnick, R.L. & Fountain, D.M., 1995. Nature and composition of the continental crust: a lower crustal perspective, *Rev. Geophys.,* **33,** 267–309.

Rybach, L., 1986. Amount and significance of radioactive heat sources in sediments, in *Thermal Modelling in Sedimentary Basins, Collections Colloques et Seminaires 44,* pp. 311–322, ed. Burrus, J., Editions Technip, Paris.

Şengör, A.M.C. & Natal'in, B.A., 2001. Rifts of the world, in *Mantle Plumes: Their Identification Through Time,* pp. 389–482, eds Ernst, R.E. & Buchan, K.L., Geological Society of America Special Paper 352.

Shapiro, N.M. & Ritzwoller, M.H., 2002. Monte Carlo inversion for a global shear-velocity model of the crust and upper mantle, *Geophys. J. Int.,* **151,** 88–105.

Shapiro, N.M. & Ritzwoller, M.H., 2004. Inferring surface heat flux distributions guided by a global seismic model: particular application to Antarctica, *Earth planet. Sci. Lett.,* **223,** 213–224.

Siebert, L. & Simkin, T., 2002. Volcanoes of the world: an illustrated catalog of holocene volcanoes and their eruptions, Tech. Rep. GVP-3, Smithsonian Institution, Global Volcanism Program Digital Information Series, http://www.volcano.si.edu/world/, last accessed January 18, 2009.

Simmons, N.A., Forte, A.M. & Grand, S.P., 2009. Joint seismic, geodynamic and mineral physical constraints on three-dimensional mantle heterogeneity: implications for the relative importance of thermal

versus compositional heterogeneity, *Geophys. J. Int.,* **177,** 1284–1304, doi:10.1111/j.1365-246X.2009.04133.x.

Stein, C.A. & Stein, S., 1992. A model for the global variation in oceanic depth and heat flow with lithospheric age, *Nature,* **359,** 123–129.

Stein, C.S. & Stein, S., 1994. Constraints on hydrothermal heat flux through the oceanic lithosphere from global heat flow, *J. geophys. Res.,* **99**(B2), 3081–3096.

USGS, 1997. Geologic province and thermo-tectonic age maps, Tech. rep., U.S. Geological Survey, http://earthquake.usgs.gov/research/structure/crust/maps.php, last accessed October 22, 2009.

Vitorello, I. & Pollack, H.N., 1980. On the variation of continental heat flow with age and the thermal evolution of continents, *J. geophys. Res.,* **85,** 983–996.

Wessel, P. & Smith, W.H.F., 1991. Free software helps map and display data, *EOS, Trans. Am. geophys. Un.,* **72**(441), 445–446.

SUPPORTING INFORMATION

Additional Supporting Information may be found in the online version of this article:

Supplement. The $1^\circ \times 1^\circ$ table containing the (public) geophysical proxies, observed heat flow and results from the extrapolation methods.

Please note: Wiley-Blackwell are not responsible for the content or functionality of any supporting materials supplied by the authors. Any queries (other than missing material) should be directed to the corresponding author for the article.